




# Enhancing the high-rate performance of $\text{Li}_3\text{V}_2(\text{PO}_4)_3/\text{C}$ for Li-ion batteries via a synergistic effect of dual carbon sources

Fei Wang<sup>1,2,\*</sup> , Xiaoyu Liu<sup>2</sup>, Zhuang Liu<sup>2</sup>, and Yanming Wang<sup>2</sup>

<sup>1</sup>Information College, Huaibei Normal University, Huaibei 235000, Anhui, China

<sup>2</sup>School of Chemistry and Materials Science, Huaibei Normal University, Huaibei 235000, Anhui, China

Received: 24 May 2021

Accepted: 25 June 2021

Published online:

5 July 2021

© The Author(s), under exclusive licence to Springer Science+Business Media, LLC, part of Springer Nature 2021

## ABSTRACT

The large-scale application of Li-ion batteries requires high-performance cathode materials. Herein, a high-activity  $\text{Li}_3\text{V}_2(\text{PO}_4)_3/\text{C}$  composite cathode has been fabricated through a solid-state reaction employing dual carbon sources of poly(acrylic acid) and soluble starch. The effects of single carbon source and dual carbon sources on the physical and electrochemical properties of  $\text{Li}_3\text{V}_2(\text{PO}_4)_3/\text{C}$  are analyzed. The porous structure induced by poly(acrylic acid) and highly conductive carbon resulted from soluble starch enable the composite to achieve large discharge capacities and stable cyclability at high C-rates. At 3.0–4.3 V and 10 C, a large discharge capacity of 121 mAh g<sup>-1</sup> (nearly 91% of the theoretical capacity) can be obtained, along with high capacity retention of 88% over 1000 cycles. Furthermore, at 3.0–4.8 V, the composite also possesses larger high-rate capacities and better cyclability than other composites prepared using single carbon source. The dual carbon sources bring a synergistic effect to the enhancement of electrochemical performances of the  $\text{Li}_3\text{V}_2(\text{PO}_4)_3/\text{C}$  composite.

## 1 Introduction

The rapid development of energy storage devices and automotive applications is in urgent need of advanced Li-ion batteries (LIBs). Cathode materials confront with more challenges than the commercial graphite anode, such as enhancing the high-rate reversible capacity and cycle lifespan [1]. In comparison to olivine  $\text{LiFePO}_4$  and  $\text{LiMnPO}_4$  cathodes with one-dimensional Li-ion diffusion paths, monoclinic  $\text{Li}_3\text{V}_2(\text{PO}_4)_3$  demonstrates three-dimensional

paths for Li-ion migration, allowing fast Li-ion insertion/extraction [2–5]. Moreover, the theoretical capacity of  $\text{Li}_3\text{V}_2(\text{PO}_4)_3$  is 197 mAh g<sup>-1</sup>, which is larger than that for  $\text{LiFePO}_4$  (170 mAh g<sup>-1</sup>) and  $\text{LiMnPO}_4$  (171 mAh g<sup>-1</sup>) [6]. However, transition metal ions are divided by the phosphate groups in the crystal structure, which leads to a low electronic conductivity (*ca.* 10<sup>-7</sup> S cm<sup>-1</sup>) and thus results in slow electrochemical kinetics [7].

A common and effective strategy to enhance the electrochemical activity of  $\text{Li}_3\text{V}_2(\text{PO}_4)_3$  is the

Address correspondence to E-mail: wangfeichem@126.com

formation of carbon coated composite, thus improving the electroconductivity of the electrode [8]. Various organics and polymers, such as citric acid, starch, glucose, beta-cyclodextrin, polyacrylonitrile, polyamide, and polyvinylpyrrolidone, have been employed as carbon sources to form the amorphous conductive carbon layer [9–19]. These studies also indicate that the molecular structure of carbon resource remarkably influences the particle shape and electrical conductivity of  $\text{Li}_3\text{V}_2(\text{PO}_4)_3/\text{C}$ , thereby affects its electrochemical behavior. For example, Rui et al. [20] employed citric acid, starch, glucose, and polyvinylidene fluoride (PVDF) to fabricate the  $\text{Li}_3\text{V}_2(\text{PO}_4)_3/\text{C}$  composites. The composite using PVDF exhibits the best rate performance due to a continuous carbon network among the  $\text{Li}_3\text{V}_2(\text{PO}_4)_3$  particles. Li et al. [21] reported that the  $\text{Li}_3\text{V}_2(\text{PO}_4)_3/\text{C}$  cathodes obtained from polymer carbon precursors, including phenolic resin and PVDF, provide much larger reversible capacities than that obtained from an organic carbon precursor of glucose because of their smaller particle sizes and higher conductivities of the composites. Furthermore, another strategy is to rationally design nanostructured and porous structured  $\text{Li}_3\text{V}_2(\text{PO}_4)_3/\text{C}$  composites, which can offer shortened solid-phase diffusion pathways for  $\text{Li}^+$  ions and thus improve the high-rate capability [22–30]. Therefore, it is a feasible strategy to fabricate the high-activity  $\text{Li}_3\text{V}_2(\text{PO}_4)_3/\text{C}$  with suitable shape and microstructure by using composite carbon sources based on their respective natures and advantages. So far, only a few literatures have studied the preparation of  $\text{Li}_3\text{V}_2(\text{PO}_4)_3/\text{C}$  employing dual carbon precursors [13, 31–34]. As reported, Ding et al. [31] used polyvinylpyrrolidone and citric acid to prepare the  $\text{Li}_3\text{V}_2(\text{PO}_4)_3/\text{C}$  cathode for aqueous LIBs, and the cathode displayed a 94.9% capacity retention over 1000 cycles. As for other cathodes, Sun et al. [2] prepared the  $\text{LiFePO}_4/\text{C}$  composite using xylitol-polyvinyl alcohol as complex carbon sources, and the composite shows a large discharge capacity of  $133 \text{ mAh g}^{-1}$  at 5 C and superior cyclability (100% capacity retention after 500 cycles). Micro-agglomerated porous  $\text{LiFe}_{0.5}\text{Mn}_{0.5}\text{PO}_4/\text{C}$  prepared using sucrose and polyvinyl alcohol as composite carbon sources displayed good rate capability ( $120.1 \text{ mAh g}^{-1}$  at 5 C) and outstanding cyclability (98% capacity retention after 200 cycles at 5 C). The results indicated that a composite carbon source was favorable for the uniform carbon coating, interconnected pore

structure, and small particle size [35]. However, the combination of double carbon sources and their respective roles need to be further studied.

Herein, we adopt a solid-state reaction process to fabricate the  $\text{Li}_3\text{V}_2(\text{PO}_4)_3/\text{C}$  composite. Both a polymeric precursor of poly(acrylic acid) ( $M_w = \sim 2000$ ) and an organic precursor of soluble starch are employed as the dual carbon sources. For comparison, the similar composites are also fabricated using a single carbon precursor of poly(acrylic acid) or soluble starch, respectively. The influences of carbon source on the morphology, particle size, microstructure, electrical conductivity, and electrochemical property of  $\text{Li}_3\text{V}_2(\text{PO}_4)_3/\text{C}$  have been investigated.

## 2 Experimental section

### 2.1 Synthesis of $\text{Li}_3\text{V}_2(\text{PO}_4)_3/\text{C}$

All the chemicals were analytical grade and purchased from Aladdin Chemical Reagent Co., Ltd. (Shanghai, China). 0.5598 g  $\text{Li}_2\text{CO}_3$ , 1.1816 g  $\text{NH}_4\text{VO}_3$ , 1.7340 g  $\text{NH}_4\text{H}_2\text{PO}_4$ , 0.54 g poly(acrylic acid), and 0.17 g soluble starch were dispersed into absolute alcohol and ball milled in a zirconia vessel at 350 rpm for 8 h. The obtained mixture was dried at  $70^\circ\text{C}$  and subsequently ground in an agate mortar. The powdered precursor was heated at  $350^\circ\text{C}$  for 5 h and then annealed at  $800^\circ\text{C}$  for 8 h in argon flow. After cooling naturally, the product was obtained and denoted as LVP/C–PAA/SS. For the synthesis of other products with single carbon source, poly(acrylic acid) (0.89 g) was used to synthesize LVP/C–PAA, and soluble starch (0.43 g) was used to prepare LVP/C–SS in a similar manner.

### 2.2 Physical characterization

The phase analysis was conducted on an X-ray diffractometer (XRD, Rigaku ultima IV). The sample morphology, particle porosity, and conductive carbon distribution were studied using a scanning electron microscope (SEM, Phenom Pro) and transmission electron microscope (TEM, Tecnai G2 F30). The carbon structure and content in the composites were evaluated with a Raman microscope (Thermo DRX) and elemental analyzer (Vario Micro Cube), respectively. Nitrogen adsorption–desorption measurement was pursued using a V-Sorb 2800TP

instrument. The particle size distributions of the samples were determined by a Zetasizer Nano analyzer.

### 2.3 Electrochemical assessment

CR2016 coin cells were assembled with the metallic lithium anode, polypropylene separator, 1 M LiPF<sub>6</sub> in dimethyl carbonate/ethylene carbonate (1:1, v/v) electrolyte, and Li<sub>3</sub>V<sub>2</sub>(PO<sub>4</sub>)<sub>3</sub>/C cathode. The as-prepared composite, acetylene black, and polyvinylidene difluoride in a mass ratio of 75:15:10 were well mixed in *N*-methyl-2-pyrrolidinone solvent and plastered on an Al foil. After drying, the electrode sheets were cut out with diameters of 12 mm with the Li<sub>3</sub>V<sub>2</sub>(PO<sub>4</sub>)<sub>3</sub> loading of ca. 1.2–1.5 mg cm<sup>-2</sup> and kept at 110 °C for 10 h in vacuum. All the cells were tested on a LANHE CT2001 battery cyler at 3.0–4.3 V and 3.0–4.8 V with different C-rates. A CHI650D electrochemical workstation was employed to test electrochemical impedance spectra (EIS, frequency range: 10<sup>5</sup>–0.01 Hz) and cyclic voltammograms (CV, scanning speed range: 0.1–0.5 mV s<sup>-1</sup>).

## 3 Results and discussion

Crystal structures of the Li<sub>3</sub>V<sub>2</sub>(PO<sub>4</sub>)<sub>3</sub>/C composites acquired from various carbon sources were analyzed by XRD, as depicted in Fig. 1. In an overall situation, the reflection peaks of all composites are similar and well match with monoclinic Li<sub>3</sub>V<sub>2</sub>(PO<sub>4</sub>)<sub>3</sub> (JCPDS card no.72–7074; space group: *P*2<sub>1</sub>/*n*) [6, 7]. No impurity phase and crystalline carbon were detected, indicating the production of a single-phase material and amorphous carbon. Moreover, carbon sources have no evident effects on the crystallinity and crystal structure of Li<sub>3</sub>V<sub>2</sub>(PO<sub>4</sub>)<sub>3</sub>.

The morphologies of the as-prepared composites examined with SEM are shown in Fig. 2a–c. All the composites exhibit granular shape with different particle sizes. The corresponding particle size distributions are demonstrated in Fig. 2d. The LVP/C–SS composite comprises well-dispersed granules with a size of ca. 60–200 nm. However, the LVP/C–PAA composite is composed of both granules and large agglomerates with a main size ranging from 90 to 350 nm. The LVP/C–PAA/SS composite has similar particles morphology to LVP/C–PAA with a main size of ca. 80–250 nm. Thus, the starch carbon source

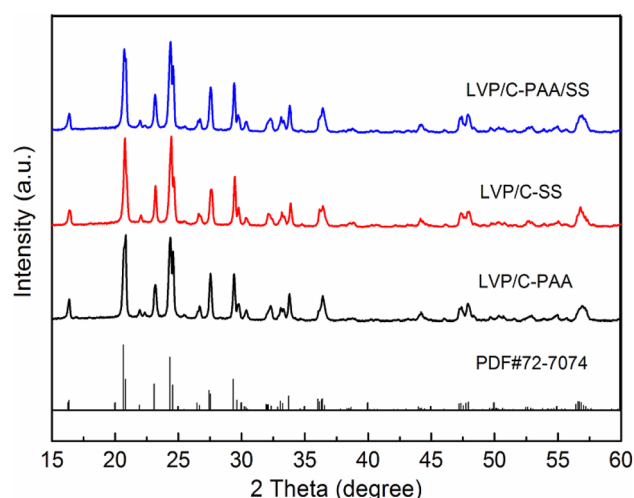
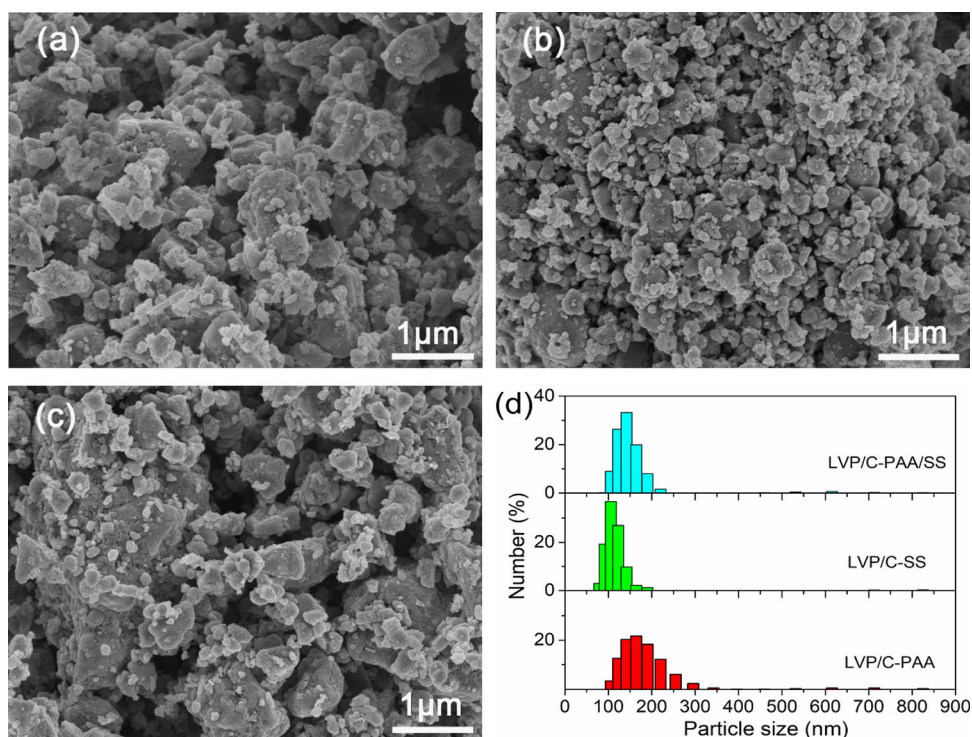


**Fig. 1** XRD patterns of the Li<sub>3</sub>V<sub>2</sub>(PO<sub>4</sub>)<sub>3</sub>/C composites

is favorable to form uniform small particles with good dispersity, while poly(acrylic acid) is prone to form partially agglomerated particles due to its polymer chains. As expected, the particle size of LVP/C–PAA/SS is remarkably influenced by a synergistic effect of dual carbon sources.

The microstructures of the three composites were further examined with TEM, as presented in Fig. 3a–c. As observed, amorphous carbon created from the thermolysis of carbon precursors covers the surface of the Li<sub>3</sub>V<sub>2</sub>(PO<sub>4</sub>)<sub>3</sub> particles and also disperses among the sample particles, thus providing an electronic transmission network on the particles surface and between adjacent Li<sub>3</sub>V<sub>2</sub>(PO<sub>4</sub>)<sub>3</sub> particles. The carbon contents are 4.81, 4.94, and 4.78 wt % for the LVP/C–PAA, LVP/C–SS, and LVP/C–PAA/SS composites, respectively. Remarkably, the LVP/C–PAA and LVP/C–PAA/SS granules represent apparent mesoporous structure, while solid structure of the LVP/C–SS granules can be observed. Furthermore, LVP/C–PAA has more mesopores than LVP/C–PAA/SS, implying that the pores result from the pyrolysis of poly(acrylic acid) polymer. Such a porous microstructure is beneficial for the infiltration of electrolyte into the active materials as well as enlargement of the electrode reaction interface, thereby improving the electrode kinetics. The electronic conductivity of carbon in the Li<sub>3</sub>V<sub>2</sub>(PO<sub>4</sub>)<sub>3</sub>/C composite remarkably affects its electrochemical performance [20, 21]. Therefore, the carbon structure was characterized by Raman spectra, as illustrated in Fig. 3d. One broad peak appearing at ca. 1357 cm<sup>-1</sup> is related to the disorder-induced D band. Another

**Fig. 2** SEM images of LVP/C–PAA (a), LVP/C–SS (b), and LVP/C–PAA/SS (c); Particle size distributions (d) of  $\text{Li}_3\text{V}_2(\text{PO}_4)_3/\text{C}$



peak emerged at ca.  $1590\text{ cm}^{-1}$  is responsible for the graphite-like G band [18, 33]. Generally speaking, a lower intensity ratio of the two bands ( $I_D/I_G$ ) implies a higher electronic conductivity of the carbon. The calculated  $I_D/I_G$  value is 0.97 for LVP/C–PAA, 0.89 for LVP/C–SS, and 0.92 for LVP/C–PAA/SS. This suggests that the carbon produced from soluble starch has better electronic conductivity than that generated from poly(acrylic acid).

Figure 4 displays the nitrogen adsorption–desorption isotherms of  $\text{Li}_3\text{V}_2(\text{PO}_4)_3/\text{C}$ . All the samples exhibit a type IV isotherm and a clear adsorption tail ( $P/P_0 > 0.9$ ), implying the existence of macropores in all the composites [35]. Moreover, LVP/C–PAA and LVP/C–PAA/SS present larger hysteresis loops at the relative pressure of 0.4–0.9 compared to LVP/C–SS, suggesting that LVP/C–PAA and LVP/C–PAA/SS possess richer mesopores than LVP/C–SS [36, 37]. The pore size distribution plots based on Barrett–Joyner–Halenda (BJH) method (insets of Fig. 4a–c) also demonstrate the mesoporous characteristic of LVP/C–PAA and LVP/C–PAA/SS. The Brunauer–Emmett–Teller (BET) specific surface areas of the LVP/C–PAA, LVP/C–SS, and LVP/C–PAA/SS composites are 27.8, 30.4, and 24.2  $\text{m}^2\text{ g}^{-1}$ , respectively. Predictably, the specific surface area of  $\text{Li}_3\text{V}_2(\text{PO}_4)_3/\text{C}$  is closely related to its particle size and

pore size distribution. These data match with the SEM and TEM results.

The electrochemical behaviors of the three composites were firstly tested between 3.0 and 4.3 V. Figure 5a–c presents the voltage curves at charging/discharging rates of 0.2–20 C. At 0.2 C-rate, all the samples represent three couples of voltage plateaus at around 3.59/3.58, 3.67/3.66, and 4.08/4.05 V, associating with the extraction/reinsertion of two  $\text{Li}^+$  ions in three steps [38]. The charge plateau voltage gradually elevates with the increase of C-rate, while the discharge plateau voltage decreases for all the composites due to the strengthened electrochemical polarization. Note that LVP/C–PAA exhibits smaller voltage hysteresis than LVP/C–SS because of its porous structure characteristics. For example, the voltage difference between charge and discharge plateaus during the removal/reinsertion of the second lithium at 20 C for LVP/C–PAA, LVP/C–SS, and LVP/C–PAA/SS is 0.21, 0.29, and 0.26 V, respectively. The rate capabilities of the three composites are compared in Fig. 5d. At 0.2 C-rate, the discharge capacities of LVP/C–PAA, LVP/C–SS, and LVP/C–PAA/SS are 126, 130, and 128  $\text{mAh g}^{-1}$ , respectively. The largest capacity of LVP/C–SS is induced by the small particle size and high electronic conduction. Nevertheless, the capacity of LVP/C–SS decays

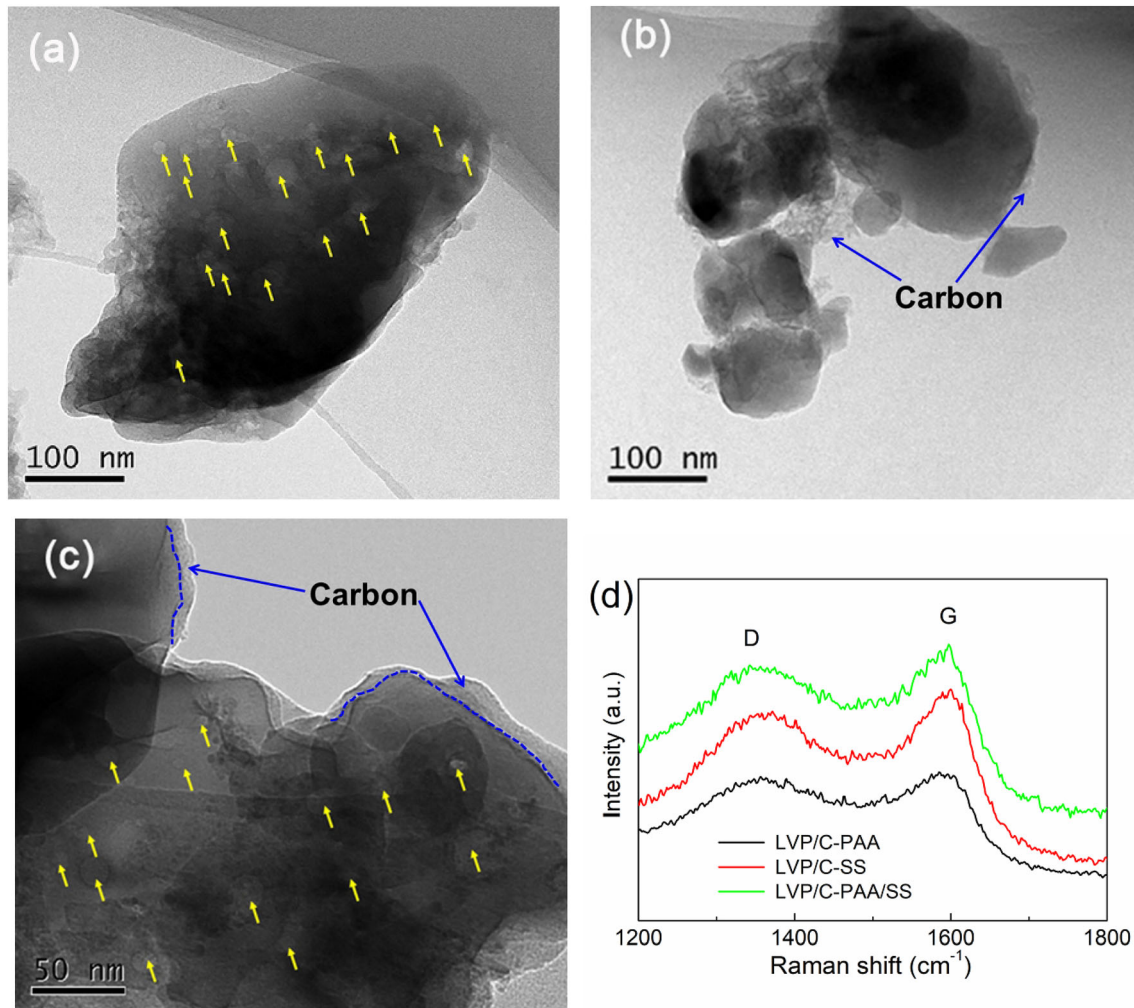


**Fig. 3** TEM images of LVP/C-PAA (a), LVP/C-SS (b), and LVP/C-PAA/SS (c); Raman spectra (d) of  $\text{Li}_3\text{V}_2(\text{PO}_4)_3/\text{C}$

rapidly with increasing C-rate. In contrast, LVP/C-PAA and LVP/C-PAA/SS exhibit superior capacity keeping ability. As the C-rate varies from 0.5 C to 10 C, the discharge capacity of LVP/C-SS is reduced by  $23 \text{ mAh g}^{-1}$ , against  $2 \text{ mAh g}^{-1}$  for LVP/C-PAA and  $5 \text{ mAh g}^{-1}$  for LVP/C-PAA/SS. The porous structure of LVP/C-PAA and LVP/C-PAA/SS provides short pathways for ionic solid-phase transport, which can accelerate electrode kinetics and thereby enhance the rate capability. Under a considerable rate of 20 C, the reversible capacity reaches  $113 \text{ mAh g}^{-1}$  for LVP/C-PAA and  $116 \text{ mAh g}^{-1}$  for LVP/C-PAA/SS, whereas it only reaches  $95 \text{ mAh g}^{-1}$  for LVP/C-SS. As observed, LVP/C-PAA/SS delivers larger capacities than the other two composites in the C-rate range of 2–20 C, suggesting that the porous structure and conductive carbon nature in the composite mainly affect the high-rate behavior of  $\text{Li}_3\text{V}_2(\text{PO}_4)_3$ .

Figure 5e and f shows the cycling performances of the three composites. As presented in Fig. 5e, the initial discharge capacities of LVP/C-PAA, LVP/C-SS, and LVP/C-PAA/SS at 1 C are 118, 122, and 123  $\text{mAh g}^{-1}$ , respectively. The capacities maintain 106, 89, and 116  $\text{mAh g}^{-1}$  after 500 cycles with capacity retentions of 90, 73, and 94%, respectively. The long-term cyclability of the composites at 10 C is illustrated in Fig. 5f. The LVP/C-PAA/SS delivers the largest initial discharge capacity of  $121 \text{ mAh g}^{-1}$  and exerts impressive capacity retention of 88% up to 1000 cycles. However, the capacity retentions of 76 and 57% are obtained for LVP/C-PAA and LVP/C-SS, respectively. The data in Fig. 5 indicate that large high-rate capacities and stable cyclability of the electrode can be achieved by the synergistic role of dual carbon sources. The comparison of the electrochemical performances between LVP/C-PAA/SS

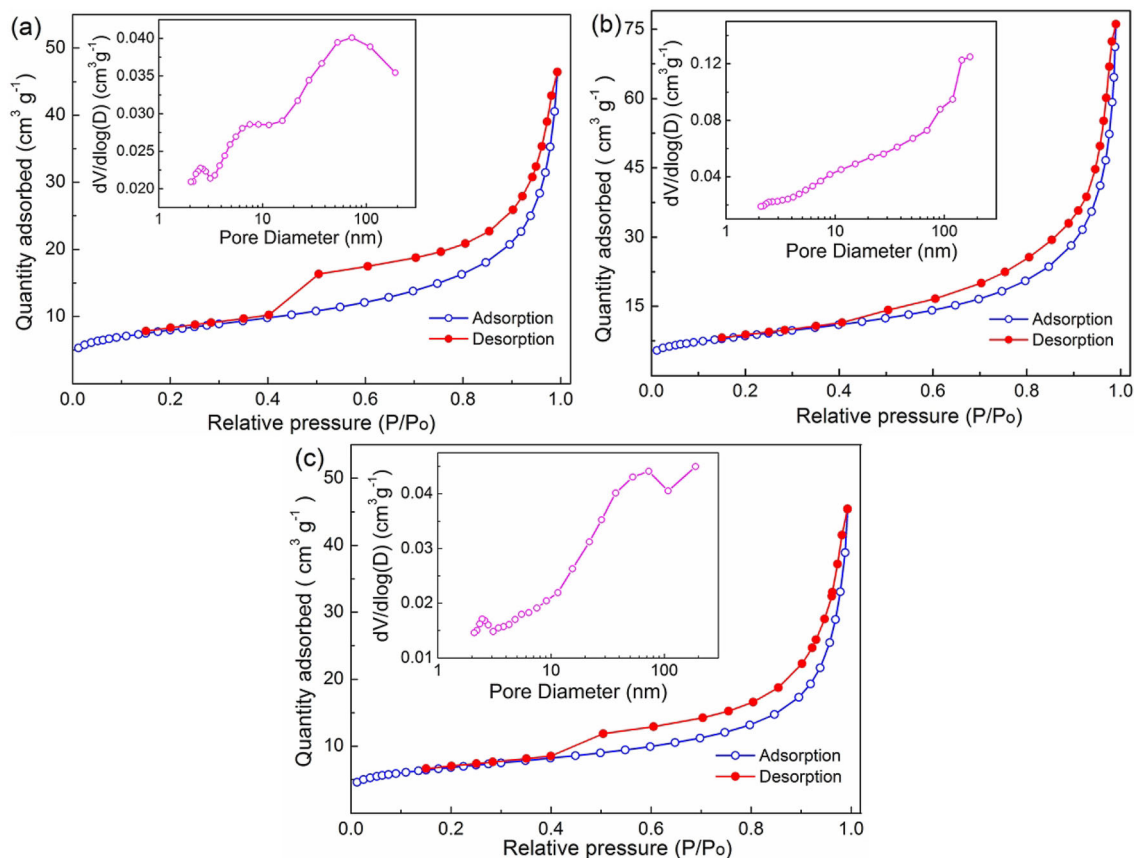


**Fig. 4**  $N_2$  adsorption–desorption isotherms and pore size distributions (inset) of the  $Li_3V_2(PO_4)_3/C$  composites

and other reported  $Li_3V_2(PO_4)_3/C$  composites is summarized in Table 1.

The electrochemical behaviors of the samples in a wide voltage region of 3.0–4.8 V were also evaluated. When the charge voltage exceeds about 4.5 V, the third lithium is released from  $Li_3V_2(PO_4)_3$  [37]. All the electrodes display the similar voltage curves at 1 C (Fig. 6a). The discharge capacities of 138, 149, and 146  $mAh\ g^{-1}$  are achieved for LVP/C–PAA, LVP/C–SS, and LVP/C–PAA/SS, respectively. As shown in Fig. 6b, LVP/C–SS demonstrates the lowest discharge capacity at 10 C, reflecting its weak electrochemical activity at high C-rate. The variations of discharge capacity with current rate for the three composites are described in Fig. 6c. Although LVP/C–SS offers the largest discharge capacity of 170  $mAh\ g^{-1}$  at 0.2 C, it shows the fastest capacity decay rate with increasing C-rate. The reversible capacity can only remain at 102  $mAh\ g^{-1}$  at 20 C, a marked 39.6% capacity decay as compared to that at 0.2 C, against 21% for LVP/C–PAA and 20% for LVP/C–PAA/SS. The cyclability of the three composites at 10 C is

presented in Fig. 6d. After 500 cycles, the capacity retention is 82% for LVP/C–PAA/SS and 80% for LVP/C–PAA, much better than that for LVP/C–SS (62%). As a result, LVP/C–PAA/SS possesses the best high-rate property among the three composites during 3.0–4.8 V cycling.

The kinetic behaviors of various electrodes were analyzed by CV tests. As shown in Fig. 7a1–c1, three pairs of oxidation/reduction peaks (labeled as  $a/a'$ ,  $b/b'$ , and  $c/c'$ ) in all the CV curves correspond to a three-step delithiation/lithiation process. The peak current ( $I_p$ ) and the square root of scan rate ( $v^{1/2}$ ) evidences a good linear relationship (Fig. 7a2–c2), demonstrating a diffusion-controlled electrode process. Thereby, the apparent Li-ion diffusion coefficient ( $D$ ,  $cm^2\ s^{-1}$ ) of the electrodes can be evaluated by Randles–Sevcik equation  $I_p = 2.69 \times 10^5 n^{3/2} A D_{Li^+}^{1/2} C v^{1/2}$  [16, 28], where  $A$ ,  $n$ , and  $C$  are the electrode surface area (1.13  $cm^2$ ), charge transfer number ( $n = 1$ ), and Li-ion concentration in the cathode ( $3.7 \times 10^{-3}\ mol\ cm^{-3}$ ) [39], respectively. The calculated values of Li-ion diffusion coefficient based

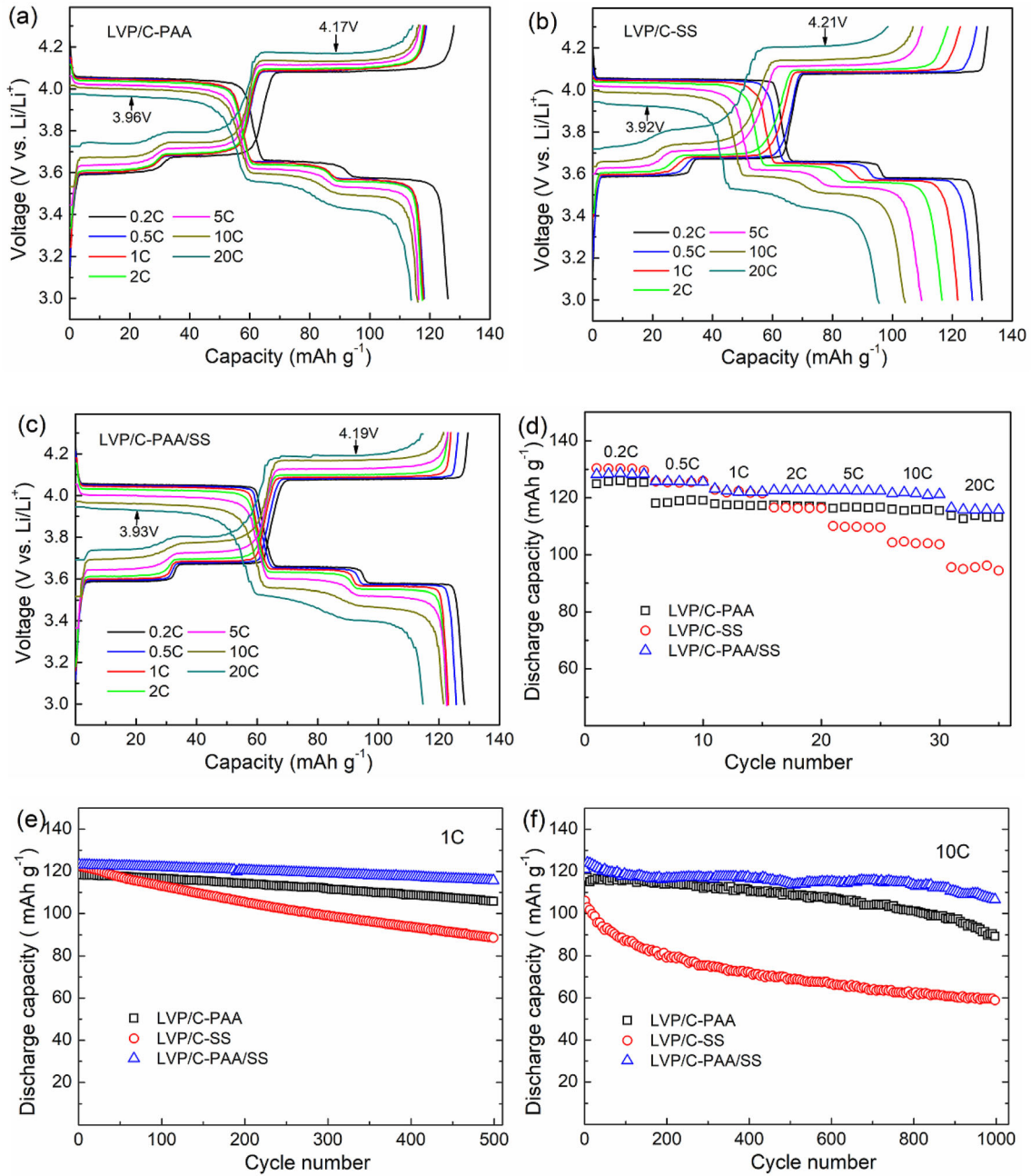


**Fig. 5** Charge–discharge curves (a–c), rate capabilities (d), and cyclabilities (e, f) of the  $\text{Li}_3\text{V}_2(\text{PO}_4)_3/\text{C}$  composites at 3.0–4.3 V

on the  $c/c'$  peaks for the three electrodes are listed in Table 2. Apparently, LVP/C–SS exerts the slowest Li-ion diffusion due to the particles of solid structure. In contrast, LVP/C–PAA shows the fastest Li-ion diffusion because of its porous structured particles. Such results agree well with the rate capability (Fig. 5d). The LVP/C–PAA/SS has a medium Li-ion diffusion coefficient among the three electrodes; despite this, it shows largest discharge capacities at

high C-rates (2–20 C). Thereby, the outstanding electrochemical performance of LVP/C–PAA/SS is not only related to its porous structure but also correlated to the carbon conductivity.

EIS tests were performed for the three electrodes after five full cycles. The obtained Nyquist plots are illustrated in Fig. 8. A semicircle at high frequencies relates to the charge transfer resistance at the electrode/electrolyte interface. A sloping line at low

**Table 1** Comparison of the electrochemical performances of LVP/C–PAA/SS with other reported  $\text{Li}_3\text{V}_2(\text{PO}_4)_3/\text{C}$  composites between 3.0 and 4.3 V

Samples	Rate capability ( $\text{mAh g}^{-1}$ )	Capacity retention	References
$\text{Li}_3\text{V}_2(\text{PO}_4)_3/\text{C}$	121 at 10 C 116 at 20 C	94% after 500 cycles at 1 C 88% after 1000 cycles at 10 C	This work
$\text{Li}_3\text{V}_2(\text{PO}_4)_3/\text{C}$	102 at 20 C	49% after 1000 cycles at 1 C	[7]
$\text{Li}_3\text{V}_2(\text{PO}_4)_3/\text{C}$	80 at 20 C	80% after 250 cycles at 20 C	[10]
$\text{Li}_3\text{V}_2(\text{PO}_4)_3/\text{C}$	118.9 at 10 C	94.7% after 100 cycles at 10 C	[16]
$\text{Li}_3\text{V}_2(\text{PO}_4)_3/\text{C}$	109 at 20 C	95.8% after 500 cycles at 1 C	[22]
$\text{Li}_3\text{V}_2(\text{PO}_4)_3/\text{C}$	85.7 at 1 C	89.4% after 500 cycles at 1 C	[28]
$\text{Li}_3\text{V}_2(\text{PO}_4)_3/\text{C}$	109.5 at 10 C	78.4% after 1000 cycles at 2 C	[30]
$\text{Li}_3\text{V}_2(\text{PO}_4)_3/\text{C}$	82.8 at 20 C	94.8% after 200 cycles at 2 C	[39]

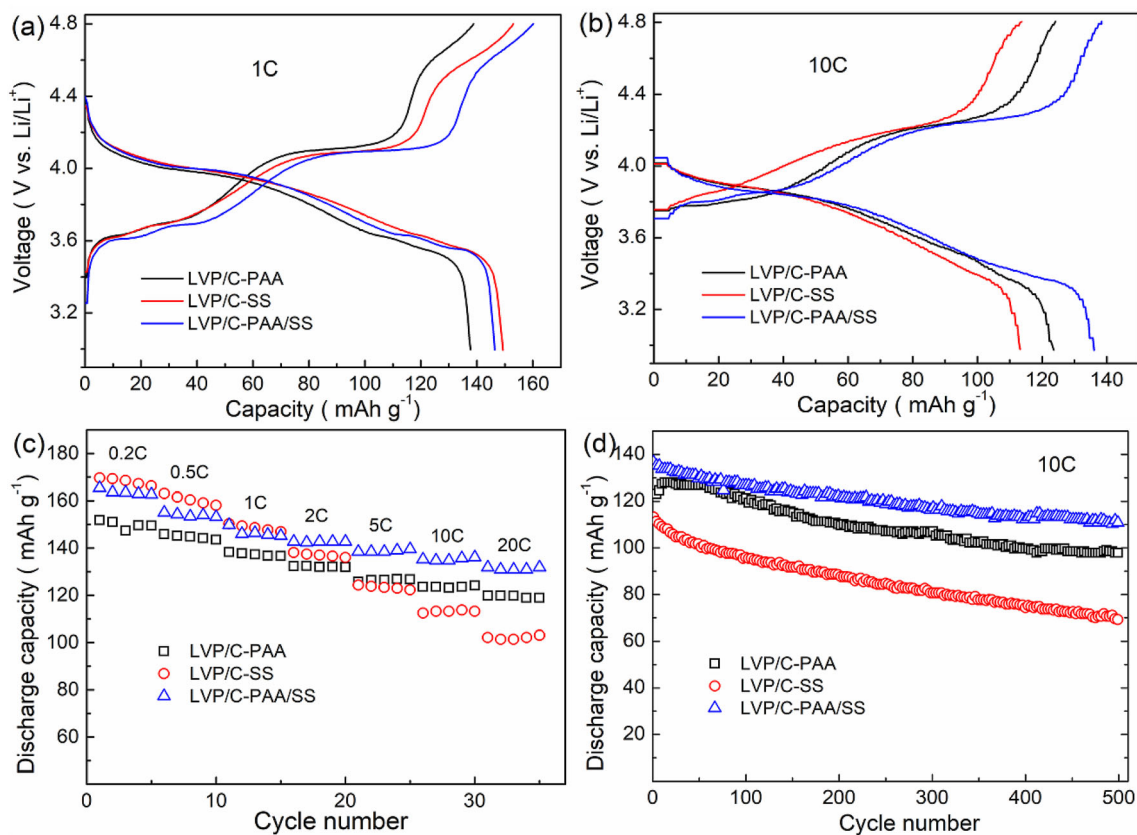


**Fig. 6** Charge–discharge curves (a, b), rate capabilities (c), and cyclabilities (d) of the  $\text{Li}_3\text{V}_2(\text{PO}_4)_3/\text{C}$  composites at 3.0–4.8 V

frequencies implies the diffusion resistance of  $\text{Li}^+$  ions inside the electrode materials. The inset in Fig. 8 is an equivalent circuit model. Here, the signs of  $R_e$ ,  $CPE$ ,  $R_{ct}$ , and  $Z_w$  represent the ohmic resistance, double-layer capacitance, charge transfer resistance, and Warburg diffusion impedance, respectively. The resistance values are summarized in Table 3. As observed, LVP/C–SS shows the smallest  $R_{ct}$ , which is largely due to the highly conductive carbon in the sample. The largest slope of the beeline for LVP/C–PAA reveals the fastest Li-ion diffusion [40, 41],

resulting from the beneficial porous structure of the composite particles. By contrast, LVP/C–PAA/SS provides moderate charge transfer and Li-diffusion resistances among the three electrodes. The EIS results are well accorded with the data of CV and rate tests.



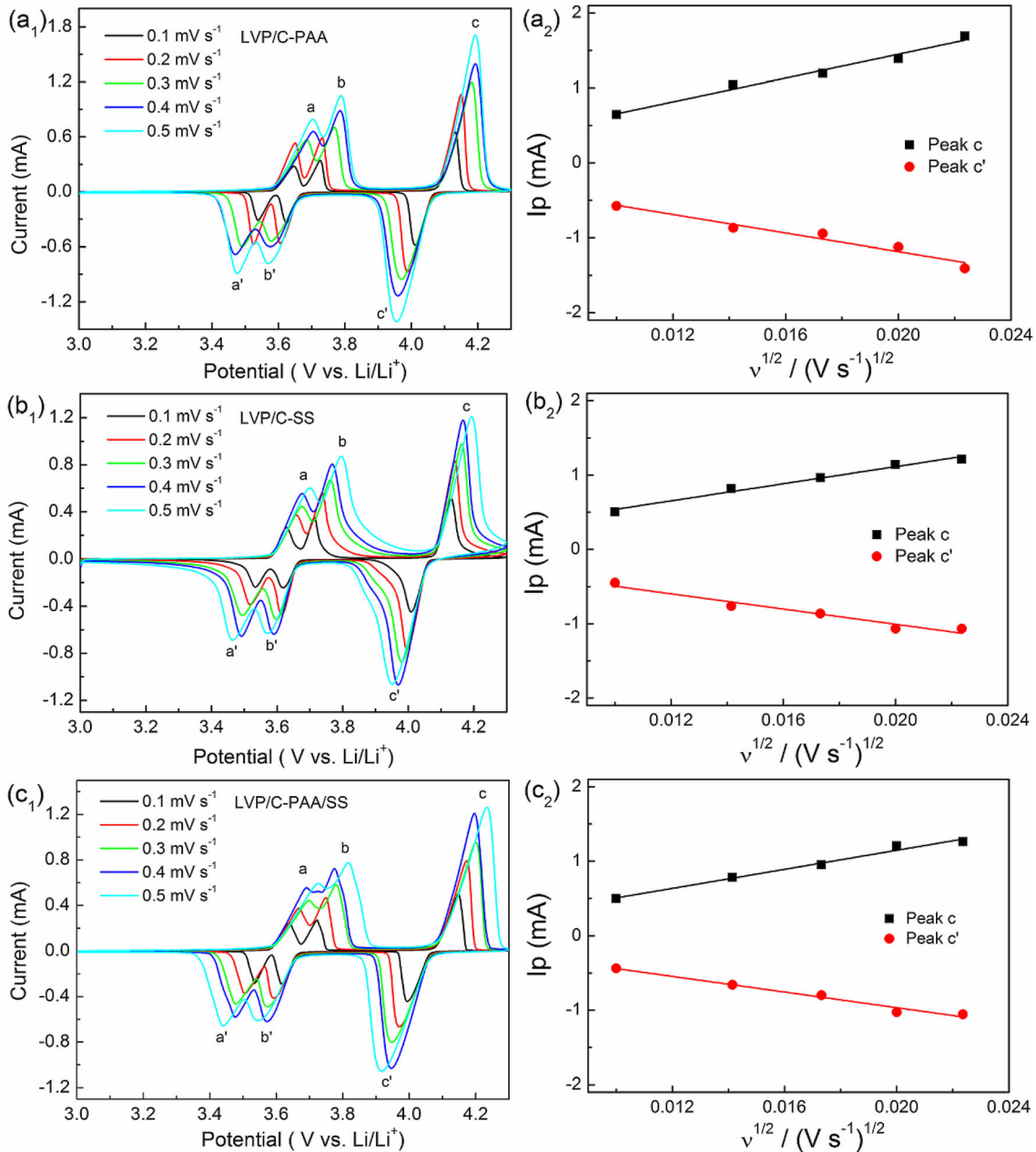


**Fig. 7** CV curves (a<sub>1</sub>–c<sub>1</sub>) and the relationship of  $I_p$  vs.  $v^{1/2}$  (a<sub>2</sub>–c<sub>2</sub>) of  $\text{Li}_3\text{V}_2(\text{PO}_4)_3/\text{C}$

**Table 2** Values of Li-ion diffusion coefficient ( $D_{\text{Li}^+}/\text{cm}^2 \text{ s}^{-1}$ )

Peaks	<i>c</i>	<i>c'</i>
LVP/C–PAA	$5.00 \times 10^{-9}$	$3.01 \times 10^{-9}$
LVP/C–SS	$2.62 \times 10^{-9}$	$2.07 \times 10^{-9}$
LVP/C–PAA/SS	$3.24 \times 10^{-9}$	$2.22 \times 10^{-9}$

### 4 Conclusions

In summary, well-crystallized  $\text{Li}_3\text{V}_2(\text{PO}_4)_3/\text{C}$  composites are facily fabricated employing diverse carbon sources. The carbon source affects the particle size, microstructure, and electrical conduction of the composite, and further influences its electrochemical performance. The LVP/C–SS composite has a small particle size and high electrical conduction, resulting in high discharge capacities at low C-rates. However,

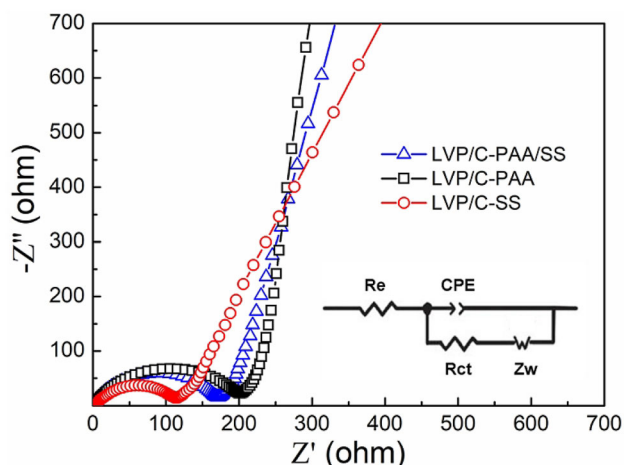


**Fig. 8** Nyquist plots and equivalent circuit (inset) of  $\text{Li}_3\text{V}_2(\text{PO}_4)_3/\text{C}$  after five cycles

**Table 3** EIS equivalent circuit fitting parameters of  $\text{Li}_3\text{V}_2(\text{PO}_4)_3/\text{C}$  composites

Samples	$R_e/\Omega$	$R_{ct}/\Omega$
LVP/C-PAA	5.07	130.7
LVP/C-SS	6.01	74.5
LVP/C-PAA/SS	3.56	121.8

the reversible capacity rapidly decreases with increasing C-rate due to the slow Li-ion diffusion within the  $\text{Li}_3\text{V}_2(\text{PO}_4)_3$  particles. Although the LVP/C-PAA composite has a large particle size and slightly low electronic conductivity, it exhibits outstanding rate performance and cyclability due to its porous structure. The dual carbon sources of poly(acrylic acid) and soluble starch exert a synergistic effect to promote the transmission of ions and electrons. Therefore, the LVP/C-PAA/SS composite displays remarkably improved electrochemical performances at high C-rates, namely, large discharge capacities and long cycle lives. The dual carbon sources strategy is in turn also possible to be employed for the preparation of other high-performance cathode materials.

## Acknowledgements

This research was funded by the Anhui Provincial Natural Science Foundation (2008085MB34) and

University Natural Science Research Project of Anhui Province (KJ2018ZD058).

## Declarations

**Conflict of interest** The authors declare that they have no conflict of interest.

## References

1. T.-F. Yi, T.-T. Wei, Y. Li, Y.-B. He, Z.-B. Wang, *Energy Storage Mater.* **26**, 165–197 (2020)
2. J. Sun, X. Ren, Z. Li, G. Liang, *Ionics* **25**, 1567–1575 (2019)
3. T.-F. Yi, Y. Li, Z. Fang, P. Cui, S. Luo, Y. Xie, *J. Materiomics* **6**, 33–44 (2020)
4. T.-F. Yi, P.-P. Peng, Z. Fang, Y.-R. Zhu, Y. Xie, S. Luo, *Compos. Part B* **175**, 107067 (2019)
5. M. Sun, X. Han, S. Chen, *Solid State Ionics* **323**, 166–171 (2018)
6. C. Liu, R. Massé, X. Nan, G. Cao, *Energy Storage Mater.* **4**, 15–58 (2016)
7. Q. Ni, L. Zheng, Y. Bai, T. Liu, H. Ren, H. Xu, C. Wu, J. Lu, *ACS Energy Lett.* **5**, 1763–1770 (2020)
8. D. Sun, C. Wu, R. Guo, Z. Liu, D. Xie, M. Zheng, B. Wang, J. Peng, H. Jiang, *Ceram. Int.* **43**, 2791–2800 (2017)
9. S. Guo, Y. Bai, Z. Geng, F. Wu, C. Wu, *J. Energy Chem.* **32**, 159–165 (2019)
10. J. Yan, Z. Tang, Y. Cao, *Ceram. Int.* **43**, 11534–11537 (2017)
11. Y. Chen, H. Chen, L. Xiao, W. Chen, H. Liao, X. Chen, K. Xiang, H. Chen, *Vacuum* **172**, 108926 (2020)
12. M. Ding, C. Cheng, Q. Wei, Y. Hu, Y. Yan, K. Dai, J. Mao, J. Guo, L. Zhang, L. Mai, *J. Energy Chem.* **53**, 124–131 (2021)
13. L. Wang, H. Liu, Z. Tang, L. Ma, X. Zhang, *J. Power Sources* **204**, 197–199 (2012)
14. Z. Cao, C. Zuo, X. Cui, X. Zhang, *Ionics* **25**, 5709–5716 (2020)
15. L. Chen, M. Jing, C. Han, H. Yang, F. Chen, H. Chen, B. Ju, F. Tu, X. Shen, *J. Mater. Sci. Mater. Electron.* **31**, 1135–1143 (2020)
16. J. Yan, Y. Cao, F. Liu, *RSC Adv.* **6**, 113228–113233 (2016)
17. H. Sun, H. Du, M. Yu, K. Huang, N. Yu, B. Geng, *Nano Res.* **12**, 1937–1942 (2019)
18. D. Zhao, L. Mo, Q. Han, L. Xie, L. Zhu, X. Cao, *Ionics* **27**, 507–515 (2021)
19. H.S. Lee, V. Ramar, S. Kuppan, M. Nagarathinam, M. Law, C. Wang, A. Tripathi, P. Balaya, *Electrochim. Acta* **372**, 137831 (2021)
20. X.H. Rui, C. Li, C.H. Chen, *Electrochim. Acta* **54**, 3374–3380 (2009)

21. L. Li, C. Fan, X. Huang, X. Zhang, S. Han, *Energy Technol.* **3**, 955–960 (2015)
22. R. Li, S. Sun, J. Liu, T. Chen, C. Dai, F. Ding, *J. Power Sources* **442**, 227231 (2019)
23. X. Liu, X. Feng, X. Xu, F. Wang, Y. Wang, *J. Sol-Gel Sci. Techn.* **86**, 343–350 (2018)
24. Y. Chen, K. Xiang, Y. Zhu, L. Xiao, W. Chen, H. Liao, X. Chen, H. Chen, *Ceram. Int.* **45**, 4980–4989 (2019)
25. R. Qin, Y. Wei, T. Zhai, H. Li, *J. Mater. Chem. A* **6**, 9737–9746 (2018)
26. Y. Li, K. Xiang, W. Zhou, Y. Zhu, L. Xiao, X. Chen, H. Chen, *J. Alloys Compd.* **766**, 54–65 (2018)
27. Y. Liao, C. Li, X. Lou, X. Hu, Y. Ning, F. Yuan, B. Chen, M. Shen, B. Hu, *Electrochim. Acta* **271**, 608–616 (2018)
28. Y. Xia, L. Yu, C. Lu, J. Zhu, Z. Xiao, J. Zhang, C. Liang, H. Huang, Y. Gan, W. Zhang, *J. Alloys Compd.* **859**, 157806 (2021)
29. J. Yang, J. Zhang, V.W. Lau, M. Park, S. Lee, J. Kim, Y.-M. Kang, *J. Phys. Chem. Lett.* **11**, 4059–4069 (2020)
30. S. Yu, A. Mertens, H. Kungl, R. Schierholz, H. Tempel, R.-A. Eichel, *Electrochim. Acta* **232**, 310–322 (2017)
31. M. Ding, M. Zhao, H. Gong, Q. Zheng, X. Song, *Ind. Eng. Chem. Res.* **58**, 790–797 (2019)
32. S. Zhang, Q. Gu, S. Tan, L. Zhao, *J. Alloys Compd.* **802**, 583–590 (2019)
33. C.-C. Yang, S.-H. Kung, S.J. Lin, W.-C. Chien, *J. Power Sources* **251**, 296–304 (2014)
34. Q. Kuang, Y. Zhao, *J. Power Sources* **216**, 33–35 (2012)
35. H. Zhuang, Y. Bao, Y. Nie, Y. Qian, Y. Deng, G. Chen, *Electrochim. Acta* **314**, 102–114 (2019)
36. Q.-Z. Ou, Y. Tang, Y.-J. Zhong, X.-D. Guo, B.-H. Zhong, H. Liu, M.-Z. Chen, *Electrochim. Acta* **137**, 489–496 (2014)
37. L. Zhang, H. Xiang, Z. Li, H. Wang, *J. Power Sources* **203**, 121–125 (2012)
38. W. Oh, H. Park, B.-S. Jin, R. Thangavel, W.-S. Yoon, *J. Mater. Chem. A* **8**, 10331–10336 (2020)
39. Q. Liu, F. Yang, S. Wang, L. Feng, W. Zhang, H. Wei, *Electrochim. Acta* **111**, 903–908 (2013)
40. B.Z. Li, Y. Wang, L. Xue, X.P. Li, W.S. Li, *J. Power Sources* **232**, 12–16 (2013)
41. T.-F. Yi, J.-P. Qu, X. Lai, X. Han, H. Chang, Y.-R. Zhu, *Mater. Today Chem.* **19**, 100407 (2021)

**Publisher's Note** Springer Nature remains neutral with regard to jurisdictional claims in published maps and institutional affiliations.